ELSEVIER

Journal of Nuclear Materials 312 (2003) 146–155

journal of nuclear materials

www.elsevier.com/locate/jnucmat

X-ray fluorescence microtomography study of trace elements in a SiC nuclear fuel shell

M. Naghedolfeizi [a], J.-S. Chung [a], R. Morris [a], G.E. Ice [a,*], W.B. Yun [b], Z. Cai [b], B. Lai [b]

[a] *Oak Ridge National Laboratory, Metals and Ceramics Division, P.O. Box 2008, Building 4500S, MS-6118, Oak Ridge, TN 37831-6118, USA*

[b] *Argonne National Laboratory, Advanced Photon Source, Experimental Facilities Division, Argonne IL 60439, USA*

Received 21 December 2001; accepted 8 November 2002

Abstract

X-ray fluorescence microtomography has been used to measure the trace element spatial distribution in a TRISO SiC shell after exposure to 1.9×10^{25} neutrons/m^2. The bare SiC shell was prepared by laser drilling the TRISO particle and leaching away the core and C. The exposed shell was measured with an X-ray probe having a size of approximately 1×3 μm^2 on beamline 2-ID at the Advanced Photon Source. The trace element distribution in the SiC shell was reconstructed after correcting the data for artifacts arising from absorption and experimental restrictions. The trace elements were found in small (<2 μm) regions through the SiC shell and appear to have been introduced during fabrication. X-ray fluorescence microtomography is an ideal tool for this work because it is a penetrating nondestructive probe with good sensitivity to high Z trace elements in a low Z matrix and because it provides a picture of the elemental distribution in the shell.
Published by Elsevier Science B.V.

1. Introduction

TRISO fuel particles, used in high-temperature gas cooled reactors are composite structures with a nuclear fuel kernel surrounded by alternating layers designed to contain fission products and compensate for radiation damage. As shown in Fig. 1, a typical fuel particle contains an inner kernel of nuclear fuel, a low density buffer layer of pyrocarbon, a dense layer of pyrocarbon coating, an interlayer of SiC and an outer dense layer of pyrocarbon. Depending on the type of reactor core design, the fuel kernel is chosen from UCO, UC_2, ThO_2, or UO_2. In addition, fuel kernel size, the thickness of the various layers, and the overall size of the TRISO fuel particle can vary with the type of fuel kernel [1]. TRISO coated fuel particles are compacted into fuel rods or spheres. The SiC layer provides the primary barrier for both radioactive elements in the kernel and gaseous and metallic fission products. The effectiveness of this barrier layer under adverse conditions is critical to containment and has been the subject of previous studies [1,2].

The SiC barrier can be compromised by fission products during irradiation or by metallic contaminates included during fabrication into a final fuel form. The fabrication contaminates are of particular interest as the final fuel processing takes place at 1800–1950 °C, temperatures well above the threshold for reactions with metals such as Fe, Ni, and Cr. These and other metals may be introduced during handling by stainless steel tools, from contaminants in the organic resins carborized to cement the particles together for the final fuel form, or from contaminants in the graphite furnace elements.

The form and location of these impurities is of crucial importance. Little risk is present if the impurities are

* Corresponding author. Tel.: +1-865 574 2744; fax: +1-865 574 7659.
E-mail address: icege@ornl.gov (G.E. Ice).

0022-3115/03/$ - see front matter Published by Elsevier Science B.V.
doi:10.1016/S0022-3115(02)01681-1

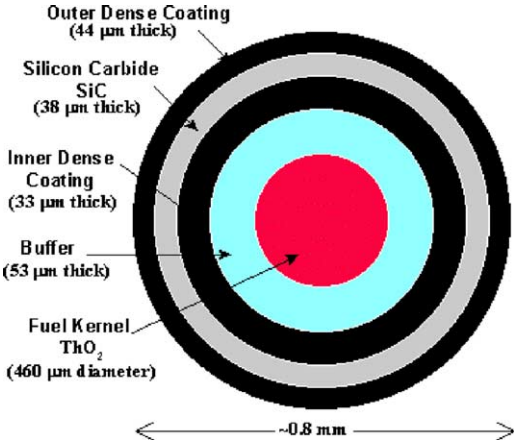

Fig. 1. Schematic of TRISO fuel element.

homogenously distributed throughout the SiC layer as the elemental concentrations are in the parts per million (ppm) range. If however, the impurities are heterogeneously distributed in the SiC layer with high local concentrations, chemical reactions between the SiC and the impurity can generate local regions of porosity, mechanical stress risers (crack initiators), or even thinning of the layer. Since the SiC layer is the major fission product barrier, this loss of integrity is not acceptable.

Current methods of quality control can only determine the average concentration of impurities and not the local concentration; thus a batch of fuel particles with a homogenous distribution of impurities in the SiC layer appears the same as a batch of fuel particles with heterogeneously distributed impurities, even though the latter may have significantly poorer performance during irradiation.

Also of interest is the location of fission products for similar reasons. Certain fission products attack the SiC layer (Pd in particular) and others will quickly diffuse into and through any faults. For example, Cs displays this behavior at the common irradiation temperatures. Clearly, localization of these attacks could more quickly result in the breach of the SiC layer and the release of the particles' radioisotope inventory. Current methods of examining the SiC layer for this behavior involves the laborious preparation of scanning electron microscope mounts and are limited to only a few cross sections though the particle. A rapid way of obtaining a three dimensional view of SiC layer fission product inventories would greatly aid the fuel behavior investigator.

We report here on measurements of the elemental *distribution* in a SiC shell after exposure to a fluence of $\sim 10^{25}$ (neutrons/m^2). X-ray fluorescence microtomography is an ideal tool for this work because it is non-destructive, it is sensitive to heavy elements in a low Z matrix, and because it can provide a 3D picture of the elemental distribution. The observed elemental distribution can be correlated with flaws and defects in the SiC shell detected either by fluorescence tomography, or by transmission absorption or phase contrast tomography [3–5].

1.1. Previous studies and sample preparation

The shell examined came from a previous study of diffusion through SiC shells [1]. In the previous study, a total of 19 shells were exposed to varying fluences (Table 1). The C buffer layers and nuclear kernels of the TRISO particles were removed by laser drilling through the SiC and then leaching the particle in acid. The shells were repeatedly leached until the activity remained constant [1]. At this point it was assumed that any remaining

Table 1
Selected isotopes and irradiation conditions for irradiated TRISO particles.

Fuel particle ID	Kernel type	Fluence (10^{25} n/m^2)	Atoms in particles		
			Cs-137	Ce-144	Eu-154
6151-23-020-C	UC_2	6.4	9.91×10^{15}	4.95×10^{15}	1.04×10^{14}
6151-23-020-D	UC_2	6.4	1.01×10^{16}	5.58×10^{15}	1.14×10^{14}
6151-23-020-E	UC_2	3.5	7.69×10^{15}	4.37×10^{15}	1.02×10^{14}
6151-23-020-F	UC_2	3.5	7.82×10^{15}	4.39×10^{15}	9.11×10^{13}
6157-08-020-A	UCO	5.8	9.05×10^{15}	4.36×10^{15}	1.19×10^{14}
6157-08-020-B	UCO	5.8	9.14×10^{15}	4.38×10^{15}	1.05×10^{14}
6157-11-020-A	UCO	6.1	9.52×10^{15}	4.60×10^{15}	1.10×10^{14}
6157-11-020-B	UCO	6.1	9.55×10^{15}	4.89×10^{15}	1.20×10^{14}
6252-12-COMP-A[a]	ThO_2	1.9	6.81×10^{14}	1.37×10^{14}	2.96×10^{12}
6252-12-COMP-B	ThO_2	1.9	6.56×10^{14}	1.36×10^{14}	3.56×10^{12}
7544-1-COMP-A	UC_2	1.9	2.79×10^{15}	5.71×10^{14}	2.20×10^{13}
7544-1-COMP-B	UC_2	1.9	3.22×10^{15}	6.30×10^{14}	2.16×10^{13}

[a] Used in this experiment.

activity was due to daughter products that had migrated into the SiC shell. The shells were then analyzed to determine the total number of the various daughter products in each shell (Table 1). This method provides an accurate absolute measurement of the total loading of radioactive elements in a shell, but gives no information about the spatial distribution within the shell.

1.2. X-ray fluorescence microtomography

The advent of intense synchrotron radiation sources has improved the resolution of tomography into the μm regime. Although most tomographic measurements use transmission tomography methods [3–5], experiments as early as 1985 demonstrated the elemental sensitivity of fluorescence tomography to high Z trace elements in a low Z matrix [6]. These pioneering measurements of the Fe distribution in a honey bee (*Apis mellifera*) found Fe concentrations at the surface and in the abdomen of the bee with a spatial resolution of approximately 150 μm. With new X-ray focusing optics and sources, fluorescence microtomography can attain spatial resolution of 1 μm^3. Fluorescence tomography however is very slow compared to transmission tomography because the number of volume elements (voxels) which can be resolved scales roughly with the number of data points collected. In contrast, transmission tomography measures the attenuation through all translation positions simultaneously and therefore has approximately 10^6 faster collection time. Although transmission measurements are much faster, fluorescence measurements have better signal-to-noise for trace element detection [7]. In Appendix A, the relative sensitivity of transmission microtomography to fluorescence microtomography is estimated in order to justify the enormous increase in time for fluorescence measurements.

One disadvantage with fluorescence tomography is the possible overlap of fluorescence lines and the potential to saturate the energy dispersive detector with a particularly intense fluorescence line. In this first attempt to study the trace element distribution within the prepared SiC shells we were constrained to search for the L lines of Cs, Ce and Eu by limitations in the energy range of the beamline. This was not considered a problem because of the reported ultra-high purity of the native SiC shells. However as we describe below, unanticipated trace elements were detected whose K lines masked the Cs, Ce and Eu L lines and raised unanticipated questions about their origin.

2. Experiment

The experimental setup for an X-ray fluorescence tomography measurement is conceptually very simple (Fig. 2). The sample is placed on a stage that rotates and translates the sample. A detector is placed in the plane of the storage ring and at an angle that is 90° to the incident beam. This detector geometry allows efficient measurement of the characteristic fluorescence from the trace elements while minimizing the X-ray elastic and Compton scattering [7]. The elemental distribution in a slice through the sample can be reconstructed after translating the sample through the X-ray beam and rotating the sample at least 180° for every x position. Finer resolution is achieved by decreasing both the translation and rotational step size.

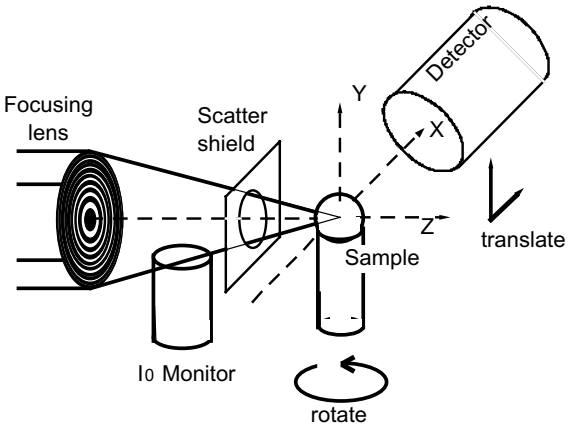

Fig. 2. Key elements of an X-ray fluorescence tomography experiment. The X-ray fluorescence is monitored while the sample is rotated and translated by a precision stage. Both the step size of the stage motions and the focal spot size of the probe beam determine the spatial resolution in the reconstructed image.

The experiment was performed on beamline 2-ID of the advanced photon source [8]. Beamline 2-ID uses a low bandpass X-ray mirror to define a beam axis, followed by a Si(1 1 1) perfect crystal monochromator and a hard X-ray zone plate. The X-ray energy was set at 10.5 keV. For this experiment a 40 cm focal length zone plate was used which produced a spot size of approximately 1×3 μm^2. The sample was epoxied to a glass fiber and sandwiched between 2 mil Kapton® tape to simplify handling. The fiber was mounted on a small goniometer head which allowed the sample to be positioned at the center-of-rotation of the rotation stage. The fuel particle sample was centered on the X-ray beam so that the translation range of the measurement passed completely through the center of the SiC shell.

Because a tomographic reconstruction requires consistent measurement conditions, the incident beam intensity was measured with an AMPTEC model XR-100T PIN diode detector with 250 eV energy resolution [9]. The detector was placed at approximately 90° scattering angle to the beam (see Fig. 2) but out of the plane of the X-ray ring (to optimize scattering efficiency).

Scatter from the air between the sample and the zone plate was monitored. This crude incident beam monitor worked well after a backscatter shield was installed between the sample and the air volume viewed by the detector. In a previous fluorescence tomography attempt with the same sample, the measurements were rendered useless for reconstruction by large and unmonitored variations in the incident beam intensity. This problem was solved with the incident beam monitor.

The quality of the reconstruction was however compromised by the limited counting time available for the measurement. For example, the stepping rate of the sample stage and the detector readout imposed an overhead of about 2 s for each measurement step. Because of the limited beam time available, a data collection scheme with 8 μm translation steps (101 translation steps) and 3° rotation steps (101 rotational steps) was used. This step size was much larger than the probe beam size (8 μm vs. 3 μm). In addition to limiting the spatial resolution, the large step size complicated the analysis since the scanning grid left gaps in the illuminated sample volume for each angle. In addition, we note that 60° of rotation was inaccessible due to the design of the rotation stage.

Before the tomographic measurements were initiated, the unfocused beam was centered on the fuel particle SiC shell to determine the detectable trace elements. The measured fluorescence spectrum is shown in Fig. 3. Regions-of-interest, ROIs, were set around the dominant fluorescence lines. Because of software limitations only 10 ROIs could be stored. The 10 ROIs stored are listed in Table 2. Unfortunately, Cs, Ce and Eu L lines lie in the region ranging from approximately 4.2 to 7 keV. This region is substantially masked by intense K fluorescence from Cr and Fe (Fig. 3). Therefore, the spatial distribution of radioactive elements, which was of great interest, was not measurable due to the large Cr and Fe concentrations in the shells.

Table 2
Measured ROIs in the fuel shell spectrum

ROI	Element	MCA channel number		Energy (KeV)
		Low	High	Center
1	Ar	248	289	2.943
2	Ca	398	475	3.68
3	Ba (lα)	656	698	4.48
4	Cr (kα)	780	845	5.41
5	Cr (kβ)	862	908	5.91
6	Fe	927	1000	6.39
7	Ni	1094	1160	7.482
8	Cu	1179	1242	8.046
9	Zn	1261	1343	8.637
10	Scattering	1556	1617	10.502

A single line scan with 2 μm step size was then made to test the data collection software and hardware and to estimate typical feature sizes. For example, the measured line scan intensity of Zn is shown in Fig. 4. As can be seen, there are numerous small Zn features through the shell, some of which are smaller than the 2 μm step resolution. The origin of this Zn is not known.

The absolute elemental concentrations were estimated by comparing the observed fluorescence signal to the X-ray elastic and Compton scattering intensities. The total scattering cross section of SiC at 90° was estimated from Ref. [10]. The beam polarization was estimated at approximately 5% and multiple scattering

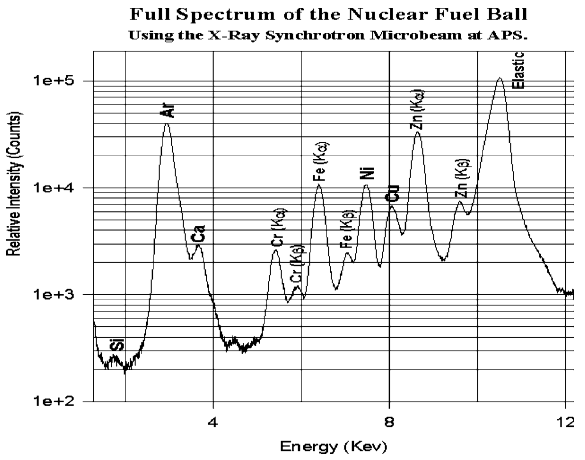

Fig. 3. Fluorescence spectrum from an unfocused beam on the fuel SiC shell.

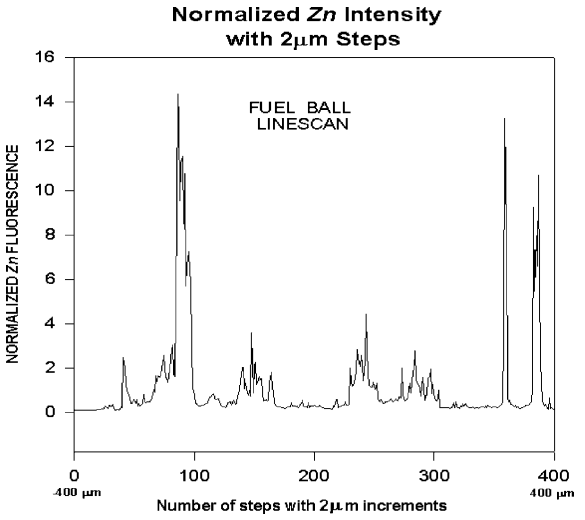

Fig. 4. Measured fluorescence intensity of Zn in a line scan experiment on TRISO fuel particle.

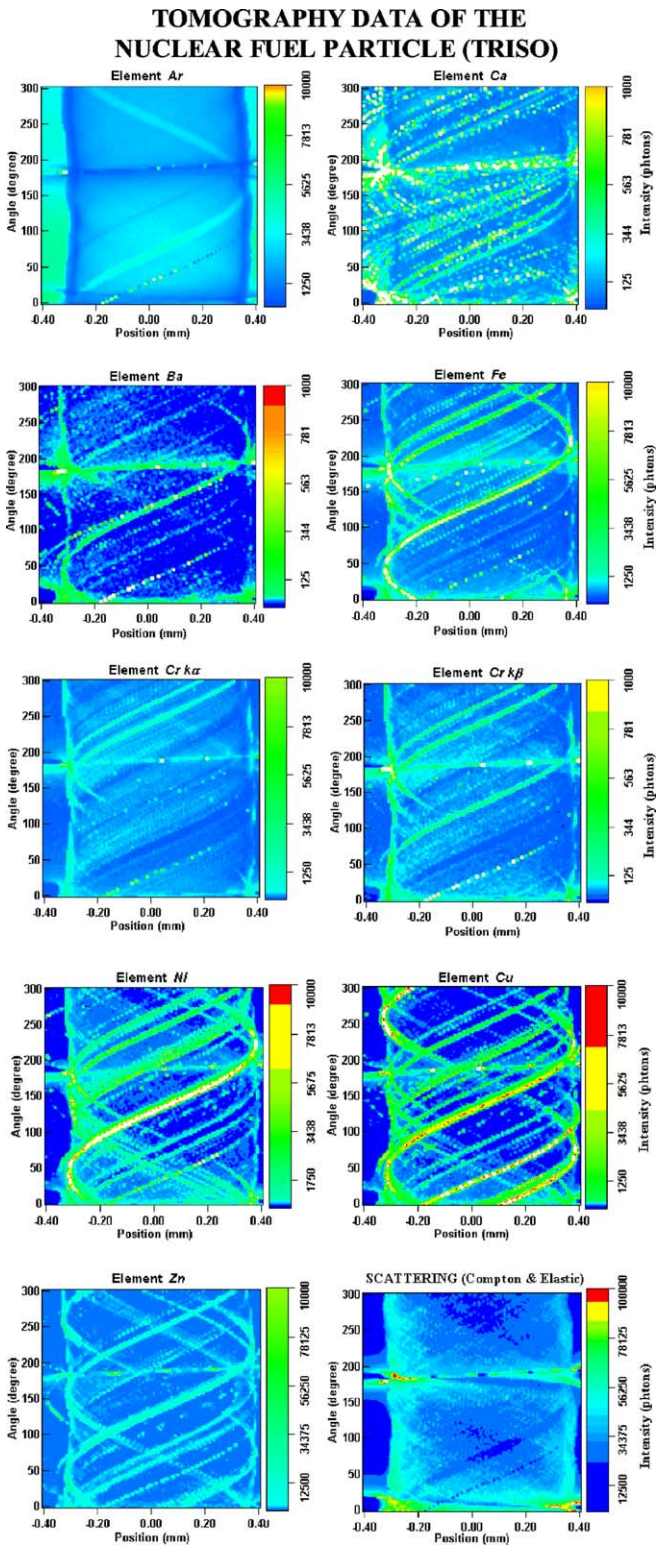

Fig. 5. Raw intensity data for the various regions of interest. The artifact due to Kapton® tape scatter is clearly seen at ~190°. Saturation artifacts are also evident in the Ar and elastic scattering patterns. Saturation artifacts can appear as decreases in intensity when the detector is paralyzed, or as increases in intensity due to energy resolution degradation at high count-rate.

and absorption were assumed to be small. With these approximations, the factor $I_0\Omega$ was determined, where I_0 is the incident beam flux in photons/s/μm^2 and Ω is the detector solid angle. The trace element concentrations were then estimated again assuming negligible absorption from the following equation.

$$I_{\text{Fluorescence}} \approx I_0\Omega(C\sigma), \tag{1}$$

Here C is the elemental concentration of the trace element and σ is the fluorescence cross-section at the incident beam energy. Self-absorption in the sample was later corrected during the tomographic reconstruction.

3. Results and experimental analysis

Plots of the ROI intensities as a function of angle and position are shown in Fig. 5. These raw images reveal a surprising amount of information about the sample. Attention to the correlated patterns in the various ROIs is also required to obtain a meaningful reconstruction of the elemental distributions. For example, the sinusoidal wave like patterns observed in the images of Fig. 5 are typical of point inhomogeneities. As seen in Fig. 5, the number of inhomogeneities varies depending on the ROI. In addition as seen in Fig. 5, the sign patterns are not always continuous. This behavior results because the

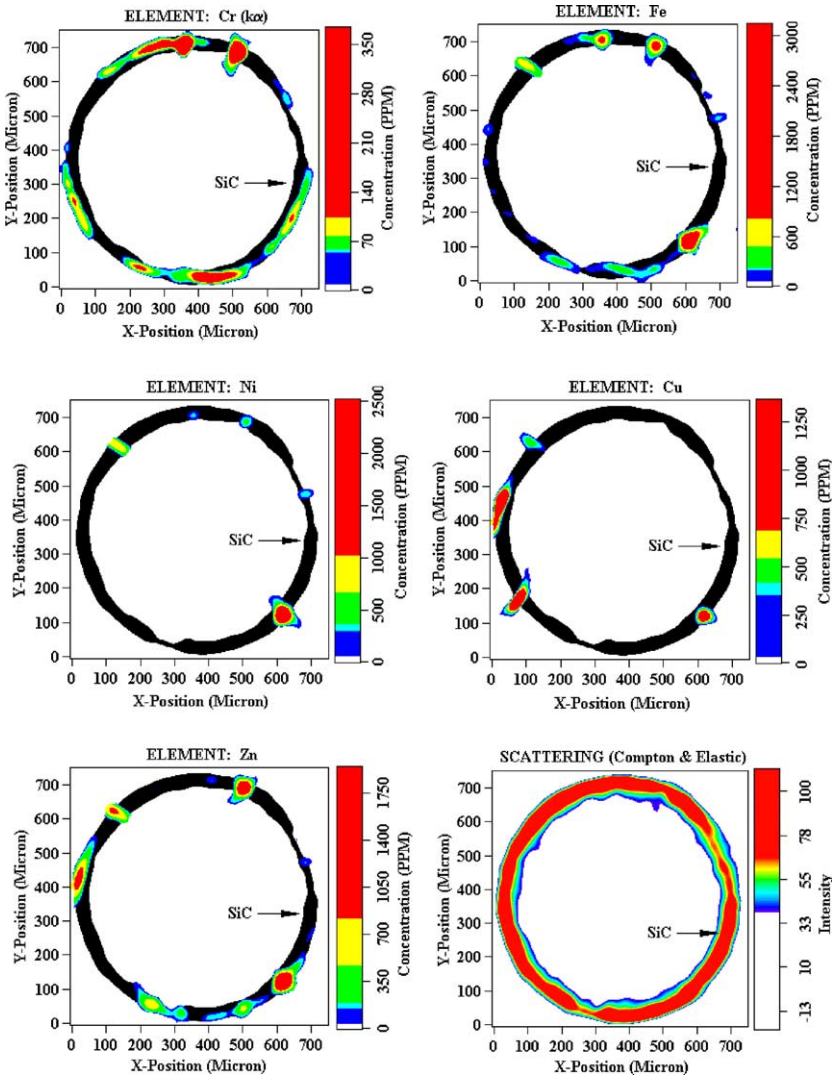

Fig. 6. Reconstructed images of the spatial distribution of trace elements with no absorption correction. The reconstructed elemental distributions are superimposed on the reconstructed shell from the elastic/Compton scattering.

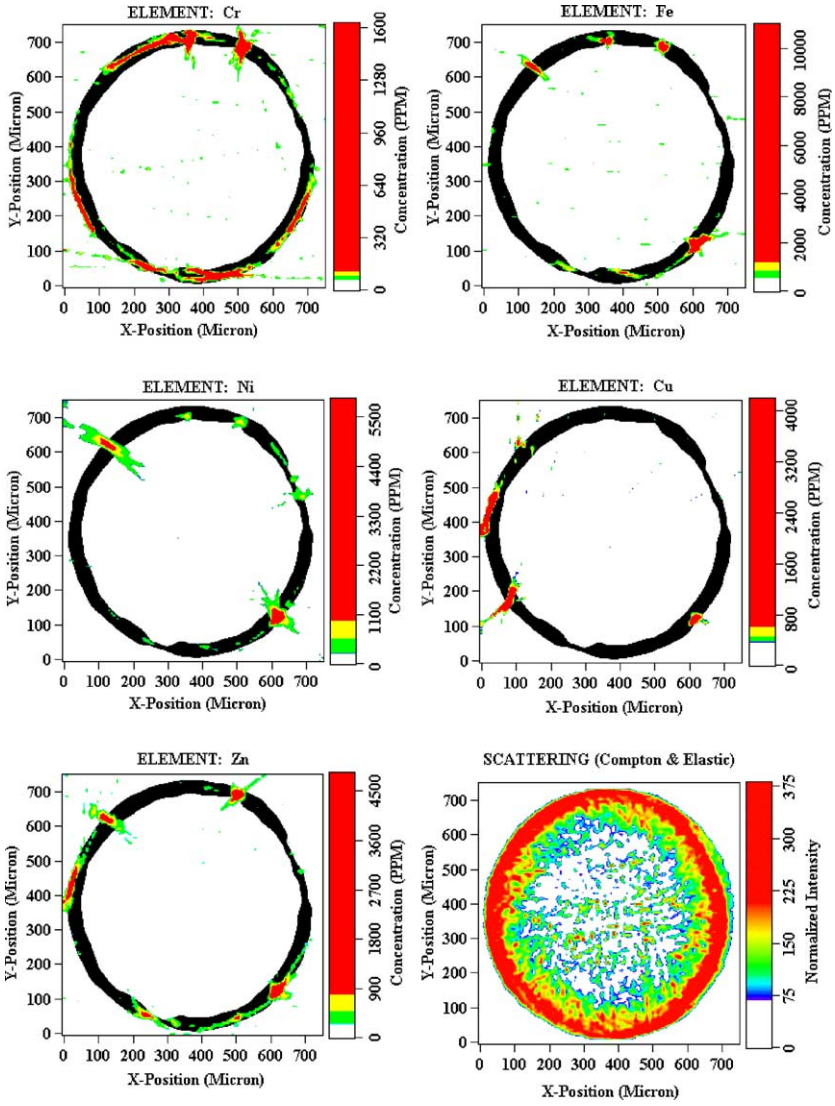

Fig. 7. Reconstructed images of the spatial distribution of trace elements with absorption correction.

step size used was larger than the convolution of the size of the X-ray probe and the inhomogeneities.

Another feature seen in Fig. 5, is a marked intensity change in all the images at $\theta \sim 190°$. This artifact arises due to scatter from the Kapton® tape used to encapsulate the sample. Near $\theta \approx 190°$ the Kapton® tape was at near glancing angle which deflected and absorbed the incident beam. These conditions produced large artifacts in the data which were removed by excluding the data points from a small angular range and averaging neighboring data points to estimate the fluorescence intensities in the missing region. Of the 10^4 data points for each ROI, approximately 25 were corrected for the effect of the Kapton® film.

In addition to the Kapton® artifact, during the measurements, the detector was occasionally saturated by an intense fluorescence signal from an unusually high concentration of one or more trace elements. Under these conditions, the ROIs from all the elements were affected. The signature for detector saturation was either a *decrease* in the intensity of many ROIs (parallized detector) or an *increase* in the intensity of many ROIs correlated with background from an intense fluorescence line. The elements responsible were identified by observing the angle/translation pattern of each element and comparing them to the intense signal coordinates. Approximately 20 points for each ROI were corrected for saturation effects using average neighboring data points.

Tomographic reconstructions were carried out, both with and without absorption correction, using the library suite RECLBL [11]. As described above, prior to the image reconstruction phase, the scanned projection data were corrected for Kapton® tape and saturation artifacts. After correcting the artifacts, the Fourier filtered back projection routine of the library was incorporated into a computer program which reconstructed the 2D images of the trace element distributions from the projection data. The mode of reconstruction was based on 360° rotations and the choice of filter was Hamming with a cutoff frequency of 0.25 Hz. As mentioned previously, the stage design limited rotations to approximately 300°. Because the reconstruction with 360° rotations appeared more robust, the missing 60° data was estimated from the 180° symmetric data.

The reconstructed spatial distributions of the monitored elements are presented in Figs. 6 and 7. Fig. 6 shows the reconstructed distribution without absorption correction and Fig. 7 shows the distribution with absorption correction. Although the fuel particle shell is only approximately 38 μm thick, absorption corrections can be large, particularly for the low energy fluorescence lines. For example, approximately 97% of the Ba fluorescence (4.48 keV) can be absorbed by the SiC shell. As a result, the trace elements distributions are most easily detected near the surface of the SiC shell.

The analysis of the images indicates that the spatial distributions of the trace elements are mostly localized at the outer edge of the SiC shell, although the spatial resolution is poor due to the large step size of the measurements. The reconstructed images with the absorption correction imply that a higher counting rate is required to improve the signal-to-noise ratio for low energy fluorescence lines. The quality of the images in reconstruction with absorption correction depends also on the selection of a proper number for intensity levels of object/background in the reconstruction routines. An elaborated trial and error procedure is required to obtain the proper number for a desired image quality. Though, at the present time, it is not possible to confidently identify the origin of the trace elements, they may have been originated from the impurities associated with the fuel, SiC, and/or fabrication processes. Measurements planned for non-irradiated fuel particles and on fuel particles exposed to different fluences will help settle this issue.

4. Conclusions and future work

X-ray microtomography is an emerging technique made practical by high brilliance X-ray sources, advanced X-ray focusing optics and high-performance X-ray detectors. X-ray brilliance in particular has been doubling every 9 months for the past 35 years. The resultant 14 orders of magnitude increase in X-ray brilliance has opened important new opportunities for materials characterization. Here, we have demonstrated that fluorescence microtomography can be a powerful tool for investigating elemental distributions in materials. The technique is non-destructive and non-invasive with high spatial resolution. It is sensitive to high Z trace elements in a low Z matrix with ppm accuracy, and has a good signal-to-noise ratio. Fluorescence microtomography can be used to simultaneously identify the elemental distributions of many trace elements. The main drawback of fluorescence microtomography is the slow data collection rate. The results of this experiment point to several ways to greatly accelerate data collection. For example, with a broad-bandpass monochromator, the fluorescence signal can be increased by 2–3 orders of magnitude with no loss in spatial resolution. With such an intense probe, it will be necessary to use wavelength dispersive spectrometers with integrating rather than single photon detectors. Such an arrangement will simultaneously increase spatial resolution and will greatly increase the sensitivity for minor trace elements of interest.

It should also be noted that in our experiment the beam energy was much lower than the K absorption edges of heavy elements such as Cs, Ce, Eu, and Ru. We therefore could not excite the K lines of these elements. The L lines are masked by overlapping K lines of less interesting trace elements. Recently reported X-ray microfocusing mirror systems will allow for significant reflectivity up to 40 keV [12]. This development will allow for unambiguous measurements of daughter products in the SiC shells.

Acknowledgements

Research sponsored in part by the Laboratory Directed Research and Development Program of the Oak Ridge National Laboratory and the Division of Materials Sciences, US Department of Energy under contract DE-AC05-96OR22464 with Lockheed Martin Energy Research Corporation. Experimental measurements were made on beamline 2-ID-CD at the Advanced Photon Source ANL which is supported by the US Department of Energy Basic Energy Science. The authors express their appreciation to Dr E.D. Specht for his technical assistance and comments.

Appendix A. Comparison of transmission contrast microtomography to fluorescence microtomography

The most sensitive way to measure elemental distributions with transmission tomography is by comparing the transmitted beam intensity between X-ray energies above and below the absorption edge of a trace element.

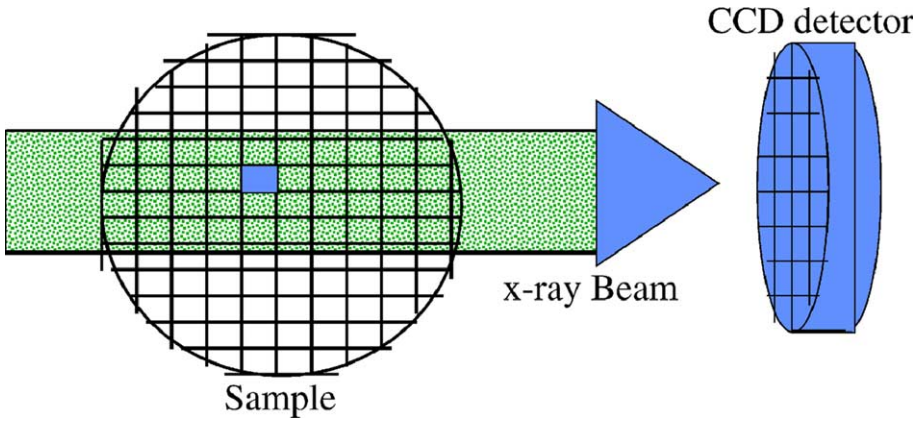

Fig. 8. Schematic of a transmission tomography experiment. The beam intensity observed by an element of the CCD detector is attenuated by all elements along the direct beam path to the detector.

In this experiment, the transmitted beam intensity is attenuated along the volume elements in the sample matrix (Fig. 8) and is detected with a high resolution CCD area detector with approximately 14–16 bits usable resolution. Typically such a detector takes about 5–10 s to readout.

We can estimate the minimum detectable limit (MDL) in the most favorable (but impractical) transmission case where the CCD detector is near the saturation limit. For example, at 10 keV, the linear absorption coefficient for $Z = 6$ is approximately 3 cm^{-1}, the linear absorption coefficient scales roughly like Z^4 and there is an increase in absorption at the K edge by an approximate factor of 8. For a small pixel with length ΔX (see Fig. 2) and with trace-element concentration C_T, the transmitted beam intensity above the K absorption edge is therefore attenuated by an additional amount $\sim e^{-7\mu_T \Delta X C_T}$ compared to the transmission below the absorption edge. Here μ_T is the trace-element linear absorption coefficient which we estimate to be $\sim 2.3 \times 10^{-3} Z^4$ (cm^{-1}). At the limit of detectability, the additional absorption is small ($e^{-\varepsilon} \sim 1 - \varepsilon$) and is at the limit of the resolution of the detector, 1.6×10^{-2} (cm^{-1}) $Z^4 \Delta X$ (cm)$C_T \sim 2^{-16}$. Changing length units to microns, we find,

$$C_T \Delta X\ (\mu m) \sim \frac{9.5\ (\mu m)}{Z^4}. \qquad (A.1)$$

For example, with $Z \sim 26$ and for feature size of approximately 1 μm the estimated detectable limit cannot be less than 20 ppm for a 5–10 s exposure. In a real measurement the detectable limit must be much higher, since the CCD must operate away from the detector saturation limit to avoid non-linear performance.

By contrast, fluorescence tomography is much more sensitive to trace elements. The estimated MDL of a modern X-ray fluorescence microbeam is ~5–80 ppb/s/μm^2 for a uniform sample [7]. Since the MDL increases as the square-root of the background, and decreases linearly with signal, the MDL of a small particle inside a larger sample will scale inversely with the ratio of particle size to sample size. The estimated MDL for fluorescence X-ray microbeam is therefore approximately 500–8000 ppb/s/μm^2, or approximately 2 orders of magnitude better than for transmission microtomography. In actual tomographic reconstruction, the elemental sensitivity is degraded slightly due to noise introduced by the reconstruction algorithm. Nevertheless, X-ray fluorescence tomography is at least 100–1000 times more sensitive to elemental distributions than transmission tomography.

References

[1] B.F. Myers, F.C. Montgomery, K.E. Partain, The transport of fission products in SiC, Doc no. 909055, GA Technologies, 1986.
[2] P. Krautwasser, G.M. Begun, Peter Angelini, J. Am. Ceram. Soc. 66 (1983) 424.
[3] See for example Q.C. Johnson, J.H. Kinney, U. Bonse, M.C. Nichols, Proc. Mater. Soc. Symp. 69 (1986) 203.
[4] J.H. Kinney, M.C. Nichols, Ann. Rev. Mater. Sci. 22 (1992) 121.
[5] Proceedings of the Workshop on High Resolution Computed Microtomography (CMT), Lawrence Berkeley National Laboratory, University of California, 12–13 August 1996.
[6] P. Boisseau, Determination of three dimensional trace element distributions by the use of monochromatic X-ray microbeams, PhD Dissertation, 1986.
[7] C.J. Sparks, in: H. Winick, S. Doniach (Eds.), Synchrotron Radiation Research, Plenum Press, New York, 1980, p. 459.
[8] W. Yun, B. Lai, D. Shu, A. Kounsary, Z. Cai, J. Barraza, D. Legnini, Rev. Sci. Instrum. 67 (1996).

[9] A.C. Huber, J.A. Pantazis, V. Jordanov, Nucl. Instrum. and Meth. B 99 (1995) 665.
[10] M.O. Krause, C.W. Nestor Jr., C.J. Sparks Jr., E. Ricci, X-ray fluorescence cross sections for K and L rays of the elements, Oak Ridge National Laboratory Technical Report ORNL-5399, 1978.
[11] R.H. Huesman, G.T. Gullberg, W.L. Greenberg, T.F. Budinger, RECLBL library users maual, Donner algorithms for reconstruction tomography, 214, Lawrence Berkeley Laboratory, University of California, 1977.
[12] G.E. Ice, J.-S. Chung, J.Z. Tischler, A. Lunt, L. Assoufid, Rev. Sci. Instrum. 71 (2000) 2635.